AIP | Applied Physics Letters

Direct observation of the structural and electronic changes of Li2MnO3 during electron irradiation

Patrick J. Phillips, Hakim Iddir, Daniel P. Abraham, and Robert F. Klie

Citation: Applied Physics Letters **105**, 113905 (2014); doi: 10.1063/1.4896264
View online: http://dx.doi.org/10.1063/1.4896264
View Table of Contents: http://scitation.aip.org/content/aip/journal/apl/105/11?ver=pdfcov
Published by the AIP Publishing

Direct observation of the structural and electronic changes of Li_2MnO_3 during electron irradiation

Patrick J. Phillips,[1] Hakim Iddir,[2] Daniel P. Abraham,[3] and Robert F. Klie[1]
[1]*Department of Physics, University of Illinois at Chicago, Chicago, Illinois 60607, USA*
[2]*Materials Science Division, Argonne National Laboratory, 9700 S. Cass Avenue, Argonne, Illinois 60439, USA*
[3]*Argonne National Laboratory, Chemical Sciences and Engineering, 9700 S. Cass Avenue, Argonne, Illinois 60439, USA*

(Received 12 August 2014; accepted 6 September 2014; published online 19 September 2014)

This study focuses on the effects of electron beam induced irradiation to the layered oxide Li_2MnO_3. Aberration-corrected scanning transmission electron microscopy and electron energy loss spectroscopy are used to characterize structural and electronic transitions in the material during irradiation, with a focus on changes in Mn valence and O content. This truly *in situ* irradiation allows for specific particle tracking, dose quantification, and real-time observation, while demonstrating many parallels to the oxide's structure evolution observed during electrochemical cycling. Furthermore, it is demonstrated that typical imaging conditions are not severe enough to induce damage to the pristine oxide. © *2014 AIP Publishing LLC*.
[http://dx.doi.org/10.1063/1.4896264]

Manganese oxide compounds are of interest to the energy industry because they are non-toxic, inexpensive, and plentiful. For example, γ-MnO_2 is widely used in primary 1.5 V Zn/MnO_2 alkaline cells, and lithium manganese oxides are commonly used as intercalation hosts in rechargeable lithium-ion cells.[1] In recent years, lithium- and manganese-rich layered oxides have gained significant interest because of their potential use in high energy density batteries.[2] Of the many compounds, Li_2MnO_3, which adopts a layered $Li[Li_{1/3}Mn_{2/3}]O_2$ structure, has gained much attention because of its high theoretical capacity (458 Ah-kg^{-1}).[3–5] However, despite being rich in lithium ions, lithium extraction from this compound is very difficult, presumably because manganese cannot be oxidized beyond 4^+ in an octahedral oxygen environment.[6] Lithium extraction is possible by the simultaneous removal of oxygen to balance the charge; this oxygen removal induces irreversible changes in the crystal structure and alters the electrochemical profile of the oxide.[7–9] In this article, we induce lithium and oxygen loss in Li_2MnO_3 through electron beam irradiation. Although electron irradiation is not a substitute for electrochemical cycling, much can be learned from the structural and electronic changes induced by the procedure. We use the electron beam irradiation to accelerate structural transformations, while simultaneously obtaining real-time microscopy and spectroscopy information on specific oxide particles at atomic resolution.

Our experiments were conducted in an aberration-corrected scanning transmission electron microscope (STEM) with electron energy loss (EEL) spectroscopy capabilities. Thus, the direct atomic-scale imaging of both heavy and light elements and the probing of local electronic structure are possible. A series of irradiations was performed on the same Li_2MnO_3 particle, oriented along the [100] zone axis direction; this allowed for atomic imaging along columns which are either pure Li and Mn or O in the pristine material. Electron microscopy observations have been presented on various layered materials (e.g., Refs. 7 and 10–13), wherein the material is imaged in its pristine state, removed from the microscope, electrochemically cycled, then inserted back into the microscope for characterization. The obvious difference in the present case is that by using the electron beam to irradiate, we can track the same particle, which is very difficult for *ex situ* experiments. Our technique has an added advantage in that any pre-existing structural differences can be characterized, and not mistakenly identified as an effect of electrochemical cycling.

The STEM images were simultaneously acquired in high/low angle annular dark field (H/LAADF) and annular bright field (ABF)—these observation modes excel in imaging: heavy elements with an intensity that approaches Z^2, strain contrast, and light elements (including H), respectively.[14–19] At each stage of irradiation, STEM images are presented in conjunction with EEL spectroscopy of the O *K*- and Mn *L*-edges, which can be used to track changes to both the O content and Mn valence. Specifically, the O *K*-edge pre-peak probes transitions from the 1s into the hybridized O 2p–Mn 3d orbitals, and thus the pre-peak intensity will generally increase with an increasing Mn valence. Additionally, the ratio of the Mn L_3/L_2 peaks is also a strong function of valence, with an increasing ratio corresponding to a decreasing valence.[20–24] In this work, both the Mn $L_{3/2}$ ratio and the energy difference between the Mn L_3- and O pre-peaks were used to quantify the Mn valence. Including the pristine state, a total of five material stages are discussed, which encompass both the structural and electronic changes induced by the electron beam.

Pristine (stage I) Li_2MnO_3 (C2/*m*) is presented in Fig. 1, viewed along the [100] zone axis, which is ideal for viewing atomic columns which are unmixed. Importantly, the pristine crystal structure is maintained all the way to the edge of the particle, with the exception of the arrowed region near its top, which shows a markedly different atomic structure (Fig. S1 (Ref. 25)). Thus, this area was avoided for all

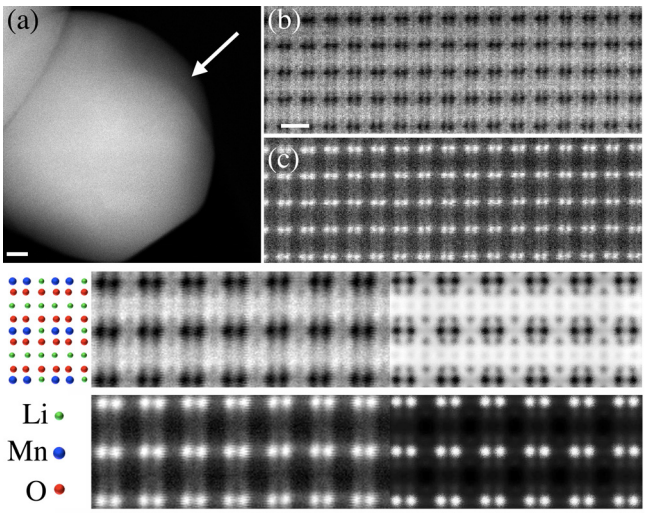

FIG. 1. (a) A low magnification HAADF image of the particle which was the focus of this study (scale bar is 20 nm); raw ABF (b) and LAADF (c) images at the atomic scale (scale bar is 0.5 nm); the lower subfigure presents a filtered/averaged experimental (left) and simulated (right) ABF and LAADF STEM image of pristine Li_2MnO_3, positioned such that the experimental image transitions approximately continuously into the simulated image. Likewise, the structural model transitions into the experimental ABF image. The complementary HAADF images do not reveal any more information than the LAADF mode, thus are omitted here, but included in the supplementary material (Fig. S2) for completeness.[25]

subsequent studies. STEM images simulated with the Kirkland software[26] are also presented in Fig. 1, using parameters that approximately match those of experimental acquisitions.[25] We note the direct imaging of Li columns, which are visible in the raw ABF image and further enhanced in the averaged image.

To irradiate the material in the STEM, a 1000 pA probe was rastered over the entire particle for a given period of time; note that the probe used for standard high resolution imaging and EELS is 19 pA, delivering an approximate dose of 1×10^7 e^-/nm^2 at a magnification of 12 Mx (scanned area $\approx 17^2$ nm^2). After an initial irradiation time of 15 min ($\approx 8.4 \times 10^7$ e^-/nm^2), no changes were obvious in the particle, so an additional 14 min of irradiation was applied ($\approx 2.6 \times 10^8$ e^-/nm^2 total). The results for this dose are presented in Fig. 2, where small "pockets" of damage appear. Atomic-scale images of these regions reveal the early stages of Mn atoms occupying the Li columns in planes both parallel and perpendicular to the Mn-Mn dumbbells in the transition metal (TM) plane of the pristine structure. Given the slight oscillation of the Mn atoms occupying the Li plane, it is plausible that both tetrahedral and octahedral sites are occupied.[27,28] This knowledge is useful in deciphering the migration mechanism of the Mn, and is under further study. The included line profiles of Fig. 2(e) acquired within a pristine (red) and a damaged (blue) TM plane highlight the movement of Mn atoms to Li sites, as the increased Li site intensity with respect to the Mn site intensity is apparent in the blue profile.

For electronic structure characterization, four spectra, normalized to the Mn L_3 edge, are presented which provide examples of stages I-IV. Spectrum I is from pristine material, while II–IV have seen the same 29 min ($\approx 2.6 \times 10^8$ e^-/nm^2) of irradiation. For this materials system, spectra from different EELS scans are difficult to properly align as both the O and Mn peaks are simultaneously changing; additionally, there exists no intrinsic energy reference (e.g., the Carbon *K*-edge). Despite, the Mn valence remaining constant between spectra I and II, their alignment based on the Mn L_3 onset energy is simply to guide the eye, while spectra III and IV were acquired within the same scan, and are considered aligned on an absolute scale. When comparing the pristine material to spectrum II, which was acquired away from any visible pockets of damage, an increase and narrowing of the O pre-peak is observed, indicating the presence of Li vacancies.[11] Spectrum III, which was acquired adjacent to the defected region of spectrum IV, shows an O pre-peak increase similar to spectrum II, and an increased Mn valence. Finally, spectrum IV shows an increased, shifted, and broadened O pre-peak, along with a decrease in the Mn valence; these changes likely result from more Li vacancy creation and the early stages of O vacancy creation. The shoulders on the left sides of the Mn L_3 peaks in spectra III/IV indicate that a convolution of the L_3 peaks for each a higher and lower valence state exists in this stage of intermediate damage (i.e., a combination of $3/4^+$); a strongly shifted Mn L_3 peak will be discussed below in regards to stage V material.

The sample was further irradiated to a total of 54 min ($\approx 5.7 \times 10^8$ e^-/nm^2 total). Following this dose, aside from an increased number of deformation pockets, the sample's appearance was similar to that following 29 min of irradiation. Subsequently, a small sample region was irradiated with the imaging probe of 19 pA such that atomic-resolution images could be acquired in real time. It is already apparent in the ABF image (Fig. 3(a)) that some of the Mn atoms have been shifted into Li columns, which is not unexpected given that the specimen had already experienced a significant dose. After approximately 3 min ($\approx 3.9 \times 10^9$ e^-/nm^2 total), a dramatic structural transformation is apparent in the center of the images, while, for example, the upper right portion of Fig. 3(d) bears some similarity to the pristine sample, with the expected Mn-Mn dumbbells. The two spectra included were taken from a line scan acquired from the center (severely damaged region) toward the right side of the image, as indicated by the red and blue lines, respectively. The extracted red spectrum represents stage V material, with an obvious shift of the Mn L-edge to lower energy and a simultaneous reduction and high-energy shift of the O *K*-edge pre-peak, reflecting significant O loss and a decrease of the Mn valence. A table summarizing all EELS results is presented in Fig. 3. Note that the doses calculated are approximate, especially those of Fig. 3, as the scanned area (magnification) was constantly being adjusted to image the real-time transformation.

Numerous publications discuss using the Mn $L_{3/2}$ ratio to determine the Mn valence, although the interpretations of these results can vary widely. For reference, and as repeatedly verified by X-ray absorption spectroscopy (XAS), the Mn valence of the pristine (stage I) material is 4^+.[8] In our study, the pristine Mn $L_{3/2}$ ratio of 1.78 is generally lower than previous reports (Refs. 21–24), although it does agree well with others.[29] The energy difference between the Mn L_3 and the O pre-peaks ("Mn L_3–O *K*" in Fig. 3) also matches well with the latter publication, although the authors note that this method works best for valences in the range 3^+–4^+.

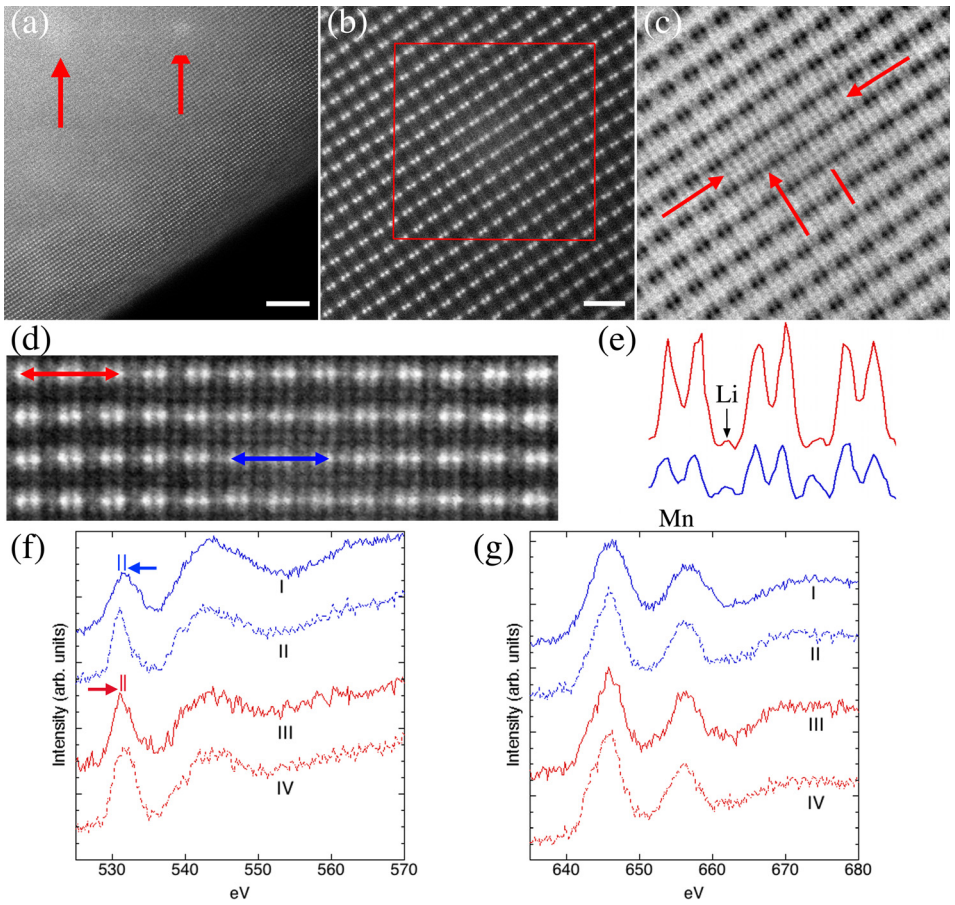

FIG. 2. (a) LAADF image with small pockets of damage arrowed—scale bar is 5 nm; (b) raw LAADF image (scale bar is 1 nm) of one of these pockets and its complementary (filtered) ABF image (c) of the indicated region; arrows denote Mn atoms occupying Li sites in both planes parallel and perpendicular to the TM planes; (d) inverted ABF image of the arrowed region in (c), along with line profiles (e) acquired from a TM plane within the damaged region (blue) or away from it (red); atomic column positions for Mn/Li in the pristine material are noted. Note that the potential oscillation of Mn atoms is most visible in the Li plane immediately above the blue line. EELS results are presented from pristine (I) and irradiated 29 min (II-IV) material of the (f) O *K*- and (g) Mn *L*-edges; the notches above the spectra pairs (I/II and III/IV) mark the approximate pre-peak centers, while arrows denote the shift in the pre-peak from the solid to the dashed spectrum in each pair, i.e., from less to more severely transformed material. Spectra I and II are aligned based on the fact that there were no Mn valence change between them. Note that the entire energy range spanning both edges was acquired within a single scan, however, the edges are plotted separately here to maximize the vertical intensity scale of each.

Thus, valences outside of this range are approximated based on extrapolating data points, and assuming that a Mn $L_{3/2}$ of 1.78 corresponds to Mn 4^+. Two values which are somewhat anomalous are starred (*) in the table. The stage III Mn L_3–O *K* value of 113.8 eV is not necessarily consistent with the trend of an increasing valence based on the work of Ref. 29, however, they do not explore valences beyond 4^+; the significant decrease in the $L_{3/2}$ ratio for stage III is a sufficient indication of the valence increase. Second, the stage V O pre-peak ratio, calculated in the same fashion as for the previous stages, actually gives a larger value than expected; this is a reflection of the inability of the calculation procedure to capture what is obvious from the spectrum, as a simple inspection clearly indicates a decreasing pre-peak, consistent with O loss.

To corroborate the EELS results, density functional theory (DFT) calculations were performed on a charge-compensated Li_2MnO_3 supercell with one row of O and two rows of Li vacancies included, as pictured in Fig. 4; with more DFT calculation details given in Ref. 25. In general, the DFT results agree well with the experimental EELS results, with the focus on characteristics such as the pre-peak intensity, the main peak intensity, the overall distribution in either set of peaks, and the separation between the pre- and the main peaks. The top (black) spectrum, acquired far from any vacancies, is taken as a bulk reference, and clearly shows a pre-peak intensity of less than that of the main peak, consistent with spectrum I from Fig. 2. The middle (blue) spectrum, taken near the Li vacancies, is consistent with experimental spectrum II, with its narrowed and increased pre-peak, thus showing the most separation between the pre- and the main peaks. The bottom (red) spectrum was taken near the O vacancies, and most notably, shows the least distinction between the pre- and the main peaks, as both become more diffuse with intensity shifting towards the other, while the pre-peak intensity also diminishes. These characteristics are most consistent with stage V material (Fig. 3), and reflect considerable O loss.

Briefly, electron beam irradiation has been used to induce structural and electronic changes in the layered Li-based oxide, Li_2MnO_3. Several important conclusions have resulted from this study, which are relevant to both the broader battery and electron microscopy communities. First, it is noted that typical imaging conditions are not sufficient to induce visible damage to the pristine material. However, it was also observed that previously damaged material will

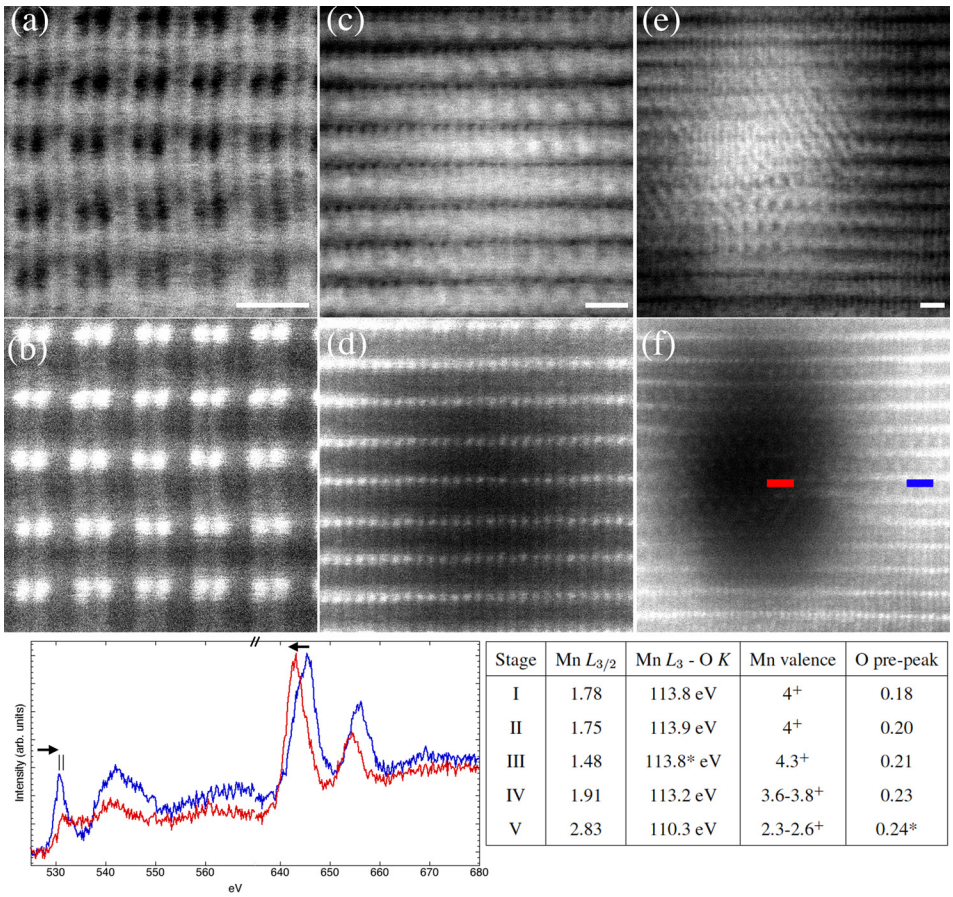

Stage	Mn $L_{3/2}$	Mn L_3 - O K	Mn valence	O pre-peak
I	1.78	113.8 eV	4^+	0.18
II	1.75	113.9 eV	4^+	0.20
III	1.48	113.8* eV	4.3^+	0.21
IV	1.91	113.2 eV	$3.6\text{-}3.8^+$	0.23
V	2.83	110.3 eV	$2.3\text{-}2.6^+$	0.24*

FIG. 3. ABF (top) and LAADF (bottom) of real-time irradiation—all scale bars 0.5 nm. (a/b) 54 min dose; (c/d) 54 min dose plus $\approx 3.3 \times 10^9$ e$^-$/nm^2; (e/f) dose of (b) plus $\approx 1.7 \times 10^9$ e$^-$/nm^2; 2D EELS line spectrum image acquired from the center (red) of the defected region toward a non-defected region (blue), as indicated. Note that the red spectrum represents stage V material. Peak shifts are again drawn from less to more severely transformed material: from blue to red in this case.

damage much more quickly than pristine material (Fig. S5 (Ref. 25)). This study is also unique in that it inherently allows for the irradiation and tracking of the same particle, which is obviously very difficult during *ex situ* electrochemical cycling experiments. Furthermore, because the particle in question was characterized prior to any irradiation, it can definitively be stated that one edge of this particle was already of a different structure prior to any electron beam induced transformation. This is important because numerous reports have identified the transformed region (following cycling) to be at the particle's edges. Of course, we acknowledge that the edges are more relevant in electrochemical experiments, and that there is no reason to expect the edges to transform preferentially in the present experiment; however, since electrochemical experiments cannot track the same particle prior to cycling, there is no way to know for sure if the edge transformations were a result of the cycling or not.

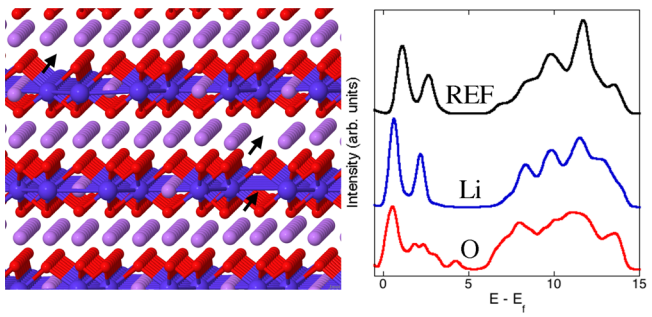

FIG. 4. The Li_2MnO_3 supercell used for the DFT calculations (Mn—blue, O—red, Li—purple) with rows of either O (left) or Li (right) vacancies arrowed, and the resulting O K-edge spectra for O atoms either far from the vacancies (black—reference), near the Li vacancies (blue) or near the O vacancies (red). Note that the intensity to the left and to the right of the text labeling each spectra represent the pre- and the main peak, respectively.

Each material stage can be attributed to an important step in its transformation during irradiation. We propose that the initial increase of the O pre-peak without any structural or $L_{3/2}$ ratio changes (stage II) is a result of the creation of Li vacancies, as confirmed by DFT. Then, prior to the expected Mn valence decrease and O vacancy creation, the material goes through stage III, wherein the Mn valence actually increases as a charge compensation mechanism; this valence increase has been previously suggested, but not demonstrated experimentally.[3,30] The other possible mechanism for charge compensation is O loss,[6] however, at this stage, the intense O pre-peak indicates this is not the case. Only after continued irradiation and significant Li vacancy creation are O vacancies created. This O loss is identified by the reduction of the O pre-peak and the Mn valence decrease, which represents stage V material. At this juncture, we speculate that, given the lack of preference for structural changes at the particle's edges, local structural instabilities (e.g., point defects) trigger the damage mechanism, which then cascades through the oxide, yielding material which will then transform more readily.

The Li_2MnO_3 was received in powder form, described in Ref. 4, dispersed in isopropyl alcohol and sonicated, and transferred to a holey Carbon grid for STEM characterization. This method is considerably gentler than, for example, methods which require ion milling or other thinning processes of bulk material. Specifically, there is no possibility of

introducing surface damage or other artifacts commonly prevalent following thinning processes. The probe-side aberration-corrected JEOL JEM-ARM200CF STEM was operated at 200 kV, with a 28 mrad semi-convergence angle and a beam current of 19 pA. Collection angles for HAADF, LAADF, and ABF were set to 110–440, 48–190, and 14–28 mrad, respectively. EELS data were treated with the multivariate statistical analysis (MSA) package for Gatan Digital Micrograph.[31] The Mn $L_{3/2}$ ratios were calculated with the second derivative method with $w\pm$ values of 2.4/2.9; O pre-peak ratios were calculated by dividing the area under the pre-peak by the area under the entire peak.

The authors acknowledge K.-B. Low and A. Nicholls of the UIC Research Resources Center, J. Bareno and R. Benedek at Argonne National Laboratory, and J.-C. Idrobo at Oak Ridge National Laboratory. Some of the computational work was conducted as part of the Applied Battery Research Program of the Office of Vehicle Technologies, U.S. Department of Energy, while computer time allocations at the Fusion Computer Facility, Argonne National Laboratory, and at EMSL Pacific Northwest National Laboratory are gratefully acknowledged. P.J.P. and R.F.K. acknowledge financial support from the Joint Center for Energy Storage Research (JCESR), an Energy Innovation Hub funded by the U.S. Department of Energy (DOE), Office of Science, Basic Energy Sciences. The UIC JEOL JEM-ARM 200CF is supported by an MRI-R^2 grant from the National Science Foundation (Grant No. DMR-0959470).

[1]M. M. Thackeray, "Manganese oxides for lithium batteries," Prog. Solid State Chem. **25**, 1–71 (1997).
[2]M. M. Thackeray, S.-H. Kang, C. S. Johnson, J. T. Vaughey, R. Benedek, and S. A. Hackney, "Li_2MnO_3-stabilized $LiMO_2$ (M = Mn, Ni, Co) electrodes for lithium-ion batteries," J. Mater. Chem. **17**, 3112–3125 (2007).
[3]P. Kalyani, S. Chitra, T. Mohan, and S. Gopukumar, "Lithium metal rechargeable cells using Li_2MnO_3 as the positive electrode," J. Power Sources **80**, 103–106 (1999).
[4]C. H. Lei, J. G. Wen, M. Sardela, J. Bareno, I. Petrov, S.-H. Kang, and D. P. Abraham, "Structural study of Li_2MnO_3 by electron microscopy," J. Mater. Sci. **44**, 5579–5587 (2009).
[5]A. Boulineau, L. Croguennec, C. Delmas, and F. Weill, "Structure of Li_2MnO_3 with different degrees of defects," Solid State Ionics **180**, 1652–1659 (2010).
[6]A. D. Robertson and P. G. Bruce, "Mechanism of electrochemical activity in Li_2MnO_3," Chem. Mater. **15**, 1984–1992 (2003).
[7]R. Wang, K. He, L. He, F. Wang, R. Xiao, L. Gu, H. Li, and L. Chen, "Atomic structure of Li_2MnO_3 after partial delithiation and relithiation," Adv. Energy Mater. **3**, 1358–1367 (2013).
[8]J. Rana, M. Stan, R. Kloepsch, J. Li, G. Schumacher, E. Welter, I. Zizak, J. Banhart, and M. Winter, "Structural changes in Li_2MnO_3 cathode material for Li-ion batteries," Adv. Energy Mater. **4**, 1300998 (2014).
[9]A. R. Armstrong, M. Holzapfel, P. Novak, C. S. Johnson, S.-H. Kang, M. M. Thackeray, and P. G. Bruce, "Demonstrating oxygen loss and associated structural reorganization in the lithium battery cathode $Li[Ni_{0.2}Li_{0.2}Mn_{0.6}]O_2$," J. Am. Chem. Soc. **128**, 8694–8698 (2006).
[10]J. Zheng, M. Gu, P. Zuo, C. Wang, and J. G. Zhang, "Corrosion/fragmentation of layered composite cathode and related capacity/voltage fading during cycling process," Nano Lett. **13**, 3824–3830 (2013).
[11]K. J. Carroll, D. Qian, C. Fell, S. Calvin, G. M. Veith, M. Chi, L. Baggetto, and Y. S. Meng, "Probing the electrode/electrolyte interface in the lithium excess layered oxide $Li_{1.2}Ni_{0.2}Mn_{0.6}O_2$," Phys. Chem. Chem. Phys. **15**, 11128 (2013).
[12]M. Gu, I. Belharouak, J. Zheng, H. Wu, J. Xiao, A. Genc, K. Amine, S. Thevuthasan, D. R. Baer, J.-G. Zhang, N. D. Browning, J. Liu, and C. Wang, "Formation of the spinel phase is the layered composite cathode used in Li-ion batteries," ACS Nano **7**, 760–767 (2013).
[13]A. Boulineau, L. Simonin, J. F. Colin, C. Bourbon, and S. Patoux, "First evidence of manganese-nickel segregation and densification upon cycling in Li-rich layered oxides for lithium batteries," Nano Lett. **13**, 3857–3863 (2013).
[14]E. J. Kirkland, R. F. Loane, and J. Silcox, "Simulation of annular dark field STEM images using a modified multislice method," Ultramicroscopy **23**, 77–96 (1987).
[15]R. F. Loane, P. Xu, and J. Silcox, "Incoherent imaging of zone axis crystals with ADF STEM," Ultramicroscopy **40**, 121–138 (1992).
[16]M. M. J. Treacy, "Optimising atomic number contrast in annular dark field images of thin films in the scanning transmission electron microscope," J. Microsc. Spectrosc. Electron. **7**, 511–523 (1982).
[17]P. J. Phillips, M. De Graef, L. Kovarik, A. Agrawal, W. Windl, and M. J. Mills, "Atomic-resolution defect contrast in low angle annular dark-field STEM," Ultramicroscopy **116**, 47–55 (2012).
[18]S. D. Findlay, N. Shibata, H. Sawada, E. Okunishi, Y. Kondo, and Y. Ikuhara, "Dynamics of annular bright field imaging in scanning transmission electron microscopy," Ultramicroscopy **110**, 903–923 (2010).
[19]Y. J. Kim, R. Tao, R. F. Klie, and D. N. Seidman, "Direct atomic-scale imaging of hydrogen and oxygen interstitials in pure niobium using atom-probe tomography and aberration-corrected scanning transmission electron microscopy," ACS Nano **7**, 732–739 (2013).
[20]M. Abbate, F. M. F. de Groot, J. C. Fuggle, A. Fujimori, O. Strebel, F. Lopez, M. Domke, G. Kaindl, G. A. Sawatzky, M. Takano *et al.*, "Controlled-valence properties of $La_{1-x}Sr_xFeO_3$ and $La_{1-x}Sr_xMnO_3$," Phys. Rev. B **46**, 4511–4519 (1992).
[21]L. Laffont and P. Gibot, "High resolution electron energy loss spectroscopy of manganese oxides: Application to Mn_3O_4 nanoparticles," Mater. Charact. **61**, 1268–1273 (2010).
[22]M. Varela, M. P. Oxley, W. Luo, J. Tao, M. Watanabe, A. R. Lupini, S. T. Pantelides, and S. J. Pennycook, "Atomic-resolution imaging of oxidation states in manganites," Phys. Rev. B **79**, 085117 (2009).
[23]B. Gilbert, B. H. Frazer, A. Belz, P. G. Conrad, K. H. Nealson, K. H. Haskel, J. C. Lang, G. Srajer, and G. De Stasio, "Multiple scattering calculations of bonding and X-ray absorption spectroscopy of manganese oxides," J. Phys. Chem. **107**, 2839–2847 (2003).
[24]Z. L. Wang, J. S. Yin, and Y. D. Jiang, "EELS analysis of cation valence states and oxygen vacancies in magnetic oxides," Micron **31**, 571–580 (2000).
[25]See supplementary material at http://dx.doi.org/10.1063/1.4896264 for more details.
[26]E. J. Kirkland, *Advanced Computing in Electron Microscopy*, 2nd ed. (Springer, 2010).
[27]S. Kim, X. Ma, S. P. Ong, and G. Ceder, "A comparison of destabilization mechanisms of the layered Na_xMO_2 and Li_xMO_2 compounds upon alkali de-intercalation," Phys. Chem. Chem. Phys. **14**, 15571–15578 (2012).
[28]J. Lee, A. Urban, X. Li, D. Su, G. Hautier, and G. Ceder, "Unlocking the potential of cation-disordered oxides for rechargeable lithium batteries," Science **343**, 519 (2014).
[29]S. Zhang, K. J. T. Livi, A.-C. Gaillot, A. T. Stone, and D. R. Veblen, "Determination of manganese valence states in (Mn^{3+}, Mn^{4+}) minerals by electron energy-loss spectroscopy," Am. Mineral. **95**, 1741–1746 (2010).
[30]T. Ohzuku, M. Nagayama, K. Tsuji, and K. Ariyoshi, "High-capacity lithium insertion materials of lithium nickel manganese oxides for advanced lithium-ion batteries: Toward rechargeable capacity more than 300 $mAhg^{-1}$," J. Mater. Chem. **21**, 10179 (2011).
[31]M. Watanabe, E. Okunishi, and K. Ishizuka, "Analysis of spectrum-imaging datasets in atomic-resolution electron microscopy," Microsc. Anal. **23**, 5–7 (2009).